J. Fluid Mech. (1987), *vol.* 177, *pp.* 437–466
Printed in Great Britain

An experimental study of the turbulence structure in smooth- and rough-wall boundary layers

By A. E. PERRY, K. L. LIM AND S. M. HENBEST
Department of Mechanical Engineering, University of Melbourne, Parkville, Victoria 3052, Australia

(Received 11 November 1985 and in revised form 10 September 1986)

The turbulence structure in zero-pressure-gradient boundary layers above smooth, rough and wavy surfaces was investigated. The mean flow, turbulence intensity and spectral data for both smooth and rough surfaces show support for the attached eddy hypothesis of Townsend (1976), the model for wall turbulence proposed by Perry & Chong (1982) and the extended version developed by Perry, Henbest & Chong (1986). Anomalies in hot-wire behaviour when measuring in the turbulent wall region of the flow were discovered and some of these have been resolved.

1. Introduction

In recent work by Perry, Henbest & Chong (1986), the turbulence structure in fully developed pipe flow was investigated in the light of Townsend's (1976) attached-eddy hypothesis, the theory of Perry & Chong (1982), the classical Kolmogorov (1941) theory and an extension of the dimensional analysis approach of Perry & Abell (1977). Encouraging support was found for the derived similarity laws. Here, zero-pressure-gradient turbulent-boundary-layer data on both smooth and rough walls are investigated in the light of the above mentioned similarity proposals, which are summarized below.

In this paper the coordinate system will be defined with x in the streamwise direction, y in the lateral direction and z normal to the wall with velocity components U_1, U_2 and U_3 respectively. Overscores denote temporal mean values and lower case letters denote instantaneous fluctuating values. The power spectral density in energy per unit streamwise wavenumber k_1 of u_i-fluctuations is $\Phi_{ii}(k_1)$, where $i = 1$, 2 or 3 (repeated indices do not denote a summation) and Φ_{ii} is normalized such that

$$\int_0^\infty \Phi_{ii}(k_1)\,\mathrm{d}k_1 = \overline{u_i^2}. \tag{1}$$

Throughout this paper the argument of the power spectral density defines the unit quantity over which the energy density is measured.

According to Perry & Chong (1982) a turbulent boundary layer can be modelled with hierarchies of coherent attached eddies which contribute to the mean vorticity and Reynolds stresses. In an extension of their work, Perry *et al.* (1986) proposed that the attached eddies are surrounded by fine-scale locally isotropic 'detached' eddies which contribute significantly to the turbulent energy dissipation but not to the mean vorticity or Reynolds shear stress. From the Biot–Savart law and spectral calculations, they showed that at a distance z from the wall, most of the contributions to u_1 and u_2 are from attached eddies of scale of order z and larger, whereas most of the contributions to u_3 are from attached eddies of scale of order z.

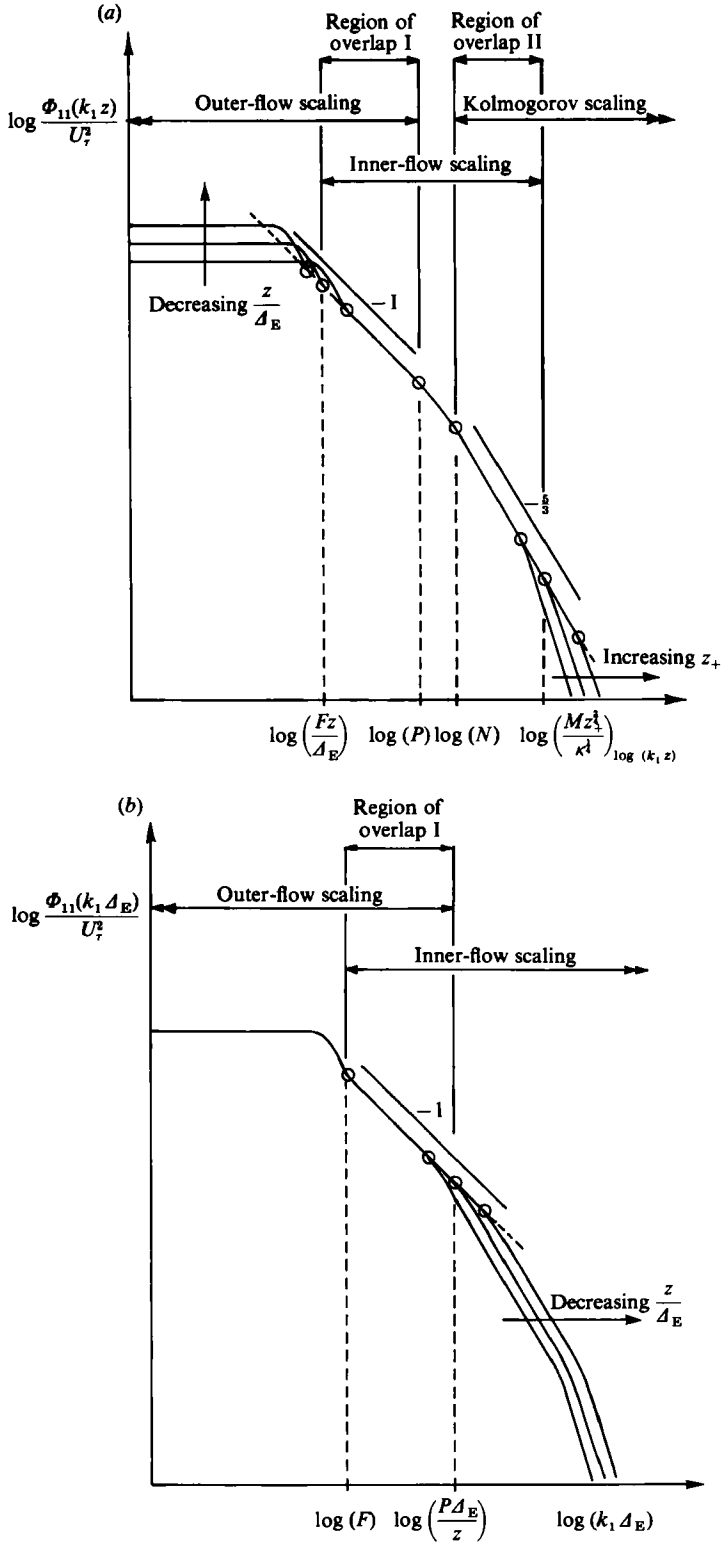

FIGURE 1. Predicted u_1-spectra (*a*) inner-flow scaling; (*b*) outer-flow scaling.

Furthermore, they showed using dimensional analysis (Perry & Abell 1977) and physical reasoning, based upon the earlier model (Perry & Chong 1982), and Townsend's attached-eddy hypothesis, that in the turbulent wall region the spectrum of u_1-velocity fluctuations should have the form shown in figure 1 (a) when scaled with 'inner flow' scaling variables (z and U_τ), and the form shown in figure 1 (b) when scaled with 'outer flow' scaling variables (Δ_E and U_τ). The turbulent wall region is defined as $\nu/U_\tau \ll z \ll \Delta_E$ for a smooth wall, where U_τ is the mean wall shear velocity, ν is the kinematic fluid viscosity and Δ_E is an integral boundary-layer thickness derived using either the Hama (1954) or the Coles (1968) velocity-defect-law formulation (see §2.3). Δ_E has a value close to the 99% boundary-layer thickness, δ_{99}. In figure 1 (a, b), P, N and M are universal constants and F is a large-scale characteristic constant. Such a constant is one that depends on the large-scale flow geometry, i.e. it depends on whether we are considering flow in a boundary layer, pipe or duct. In region of overlap I, shown in figure 1 (a, b), the spectrum follows an inverse power law, i.e.

$$\frac{\Phi_{11}(k_1\Delta_E)}{U_\tau^2} = \frac{A_1}{k_1\Delta_E}, \quad \text{or} \quad \frac{\Phi_{11}(k_1 z)}{U_\tau^2} = \frac{A_1}{k_1 z}, \tag{2}$$

where A_1 is a universal constant. In region of overlap II, shown in figure 1 (a), the spectrum follows the Kolmogorov (1941) $-\frac{5}{3}$ power law, i.e.

$$\frac{\Phi_{11}(k_1\eta)}{v^2} = \frac{K_0}{(k_1\eta)^{\frac{5}{3}}}, \quad \text{or} \quad \frac{\Phi_{11}(k_1 z)}{U_\tau^2} = \frac{K_0}{\kappa^{\frac{2}{3}}}\frac{1}{(k_1 z)^{\frac{5}{3}}}, \tag{3}$$

where $\eta = (\nu^3/\epsilon)^{\frac{1}{4}}$, $v = (\nu\epsilon)^{\frac{1}{4}}$, K_0 is the universal Kolmogorov (1941) constant and κ is the von Kármán constant. Region of overlap II is often referred to as the inertial subrange. The dissipation range begins at the end of the $-\frac{5}{3}$ power-law region at a universal value of $k_1\eta = M$ or a value of $k_1 z = (k_1 z)_p = M(\kappa)^{-\frac{1}{4}}(z_+)^{\frac{3}{4}}$, where $z_+ = zU_\tau/\nu$.

The existence of an inverse-power-law region for the streamwise velocity component in wall-bounded shear flows has been noted in the literature before (see Tchen 1953; Laufer 1954; Bremhorst & Bullock 1970; Bremhorst & Walker 1973; Hinze 1975; Perry & Abell 1977; Bullock, Cooper & Abernathy 1978; Hunt & Joubert 1979; Erm, Smits & Joubert 1986). Tchen showed that under certain conditions in homogeneous shear flow without boundaries, an inverse-power-law spectral region can occur for the streamwise velocity component only. He correlated this with the boundary-layer data of Klebanoff & Diehl (1951). The authors believe that Tchen's analysis in its present form is not applicable to wall-bounded shear flows.

Be integrating over the various u_1-spectral regions the u_1-broadband turbulence intensity distribution in the turbulent wall region is obtained, i.e.

$$\frac{\overline{u_1^2}}{U_\tau^2} = B_1 - A_1 \ln\left(\frac{z}{\Delta_E}\right) - C(z_+)^{-\frac{1}{2}}, \tag{4}$$

where C is a universal constant and B_1 is a large-scale characteristic constant.

The expected analytical forms for the u_2-motions in the turbulent wall region were shown to be similar to those for the u_1-motions because attached eddies which contribute significantly to u_1 also contribute significantly to u_2. Tchen did not obtain this result.

For the u_3-spectra no outer-flow scaling law is expected because the contributions to u_3 from the attached eddies are only from attached eddies of scale of order z. Hence, only an inner-flow scaling law and a Kolmogorov scaling law are expected for the

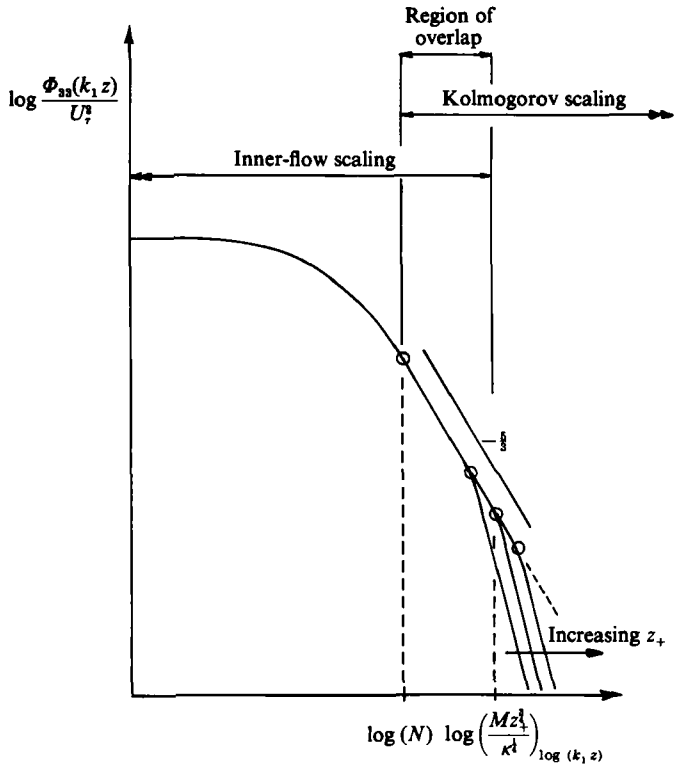

FIGURE 2. Predicted u_3-spectra, inner-flow scaling.

u_3-spectra in the turbulent wall region and should have the form shown in figure 2 when scaled with inner-flow scaling coordinates. One region of overlap exists, the inertial subrange, in which the spectrum follows a $-\frac{5}{3}$ power law. Integrating over the various u_3-spectral regions gives the u_3-broadband turbulence intensity distribution in the turbulent wall region, i.e.

$$\frac{\overline{u_3^2}}{U_\tau^2} = A_3 - \tfrac{4}{3}C(z_+)^{-\frac{1}{2}}, \tag{5}$$

where A_3 is a universal constant.

The authors believe that hierarchies of attached coherent eddies similar to those over a smooth surface also exist over a fully rough surface except that the smallest hierarchy now scales with k, the roughness scale, instead of with the Kline *et al.* (1967) scaling (see Perry & Chong 1982). For a rough wall the turbulent wall region is defined as $k \ll z \ll \Delta_E$. It is anticipated that the analysis of Perry *et al.* (1986) will also be valid for fully developed rough-wall flow and it will be seen that the data gives encouraging support to their analysis. There may be slight differences in the numerical constants obtained from the smooth-wall and the rough-wall boundary-layer data presented here owing to experimental difficulties. However, under asymptotic conditions of $\nu/U_\tau \ll z \ll \Delta_E$ and $k \ll z \ll \Delta_E$ we expect that the scaling laws for smooth and rough surfaces would be indistinguishable.

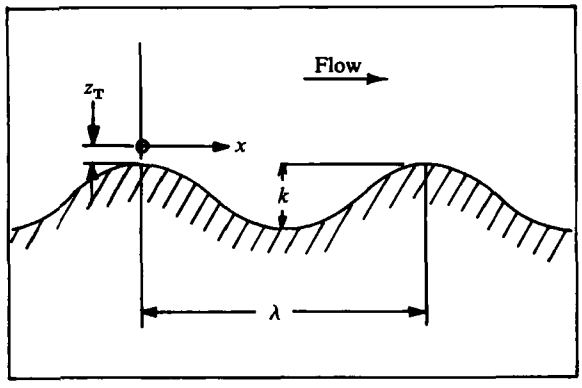

FIGURE 3. Schematic view of the wavy wall. $k = 17$ mm; $\lambda = 76$ mm.

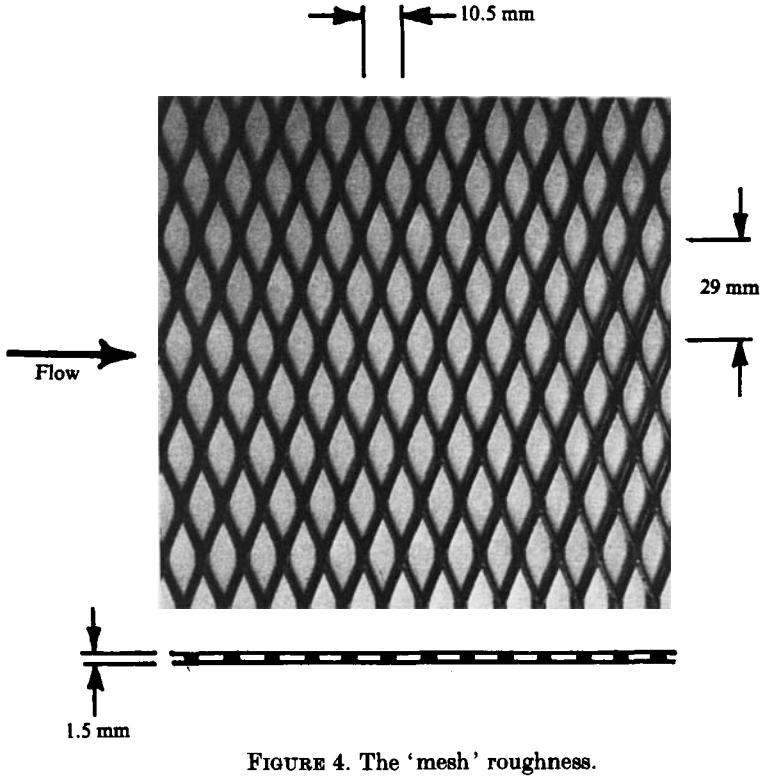

FIGURE 4. The 'mesh' roughness.

2. Apparatus

Boundary-layer flow over a two-dimensional 'wavy' surface (figure 3), a three-dimensional 'mesh' roughness (figure 4) and a smooth flat plate were investigated. The closed circuit wind tunnel used has working-section inlet dimensions of 940 mm (width) by 410 mm (height), is 6.7 m long and has an adjustable roof which was used to set a zero pressure gradient. Mounted above the working section is the 'flying hot-wire' facility described in Watmuff, Perry & Chong (1983). The measuring probe (Pitot-static or hot-wire) is mounted onto the 'flying hot-wire' sled sting during measurement. The sled can be moved along the working-section centreline enabling

measurements to be made at different streamwise locations and a stepping motor on the sled enables the probe to be traversed through the boundary layer. A separate facility enabled the probe to be traversed laterally across the working section to check for secondary flows.

Mean velocity profiles were measured using a Pitot-static probe. Presure differences were measured with a Datametrics Barocel pressure transducer model 1014A.

2.1. *Hot-wire anemometry*

All hot wires were operated in constant-temperature mode with a nominal resistance ratio of 2.0 using hot-wire anemometers similar to those detailed in Perry (1982 pp. 60–70 and Appendix C). The etched length of the 5 μm-diameter hot-wire filaments was nominally 1.2 mm and the X-wires were nominally $\pm 45°$, and where stated $\pm 60°$, to the mean flow direction. The non-linear dynamic calibration method used is described in Perry (1982 pp. 126). Signals were sampled on-line by a PDP 11/10 digital computer using a 12-bit A–D converter.

The u_1-spectra were measured with uncalibrated normal wires and the u_2- and u_3-spectra with dynamically matched, uncalibrated X-wires. The power spectral density of the hot-wire signal was calculated using a FFT-algorithm and the resulting frequency bandwidth was 0.1 Hz to 10 kHz. The spectral argument was converted from frequency f to one-dimensional streamwise wavenumber k_1 using Taylor's (1938) hypothesis of frozen turbulence, i.e. $k_1 = 2\pi f/U_c$ where U_c is the local convection velocity, which was assumed to be equal to the local mean velocity at that point in the flow. In reality, there is a spread in convection velocities at a given wavenumber and the effect of this on the inferred boundary-layer spectra obtained using Taylor's hypothesis has been examined by Perry *et al.* (1986). The spectra presented here were smoothed and then normalized using (1).

2.2. *Wall shear velocity*

In all experiments we attempted to use the X-wire Reynolds shear stresses to infer U_τ, the wall shear velocity. To test the accuracy of this method U_τ was obtained using independent methods. On a smooth wall, the Clauser-chart and Preston-tube methods are available and are known to be fairly reliable, but on a rough wall no really reliable method exists.

On rough walls, difficulties arise because we do not know the effective origin of the boundary layer, (i.e. the apparent position of $z = 0$ relative to the tops of the roughness elements, see insert in figure 5), preventing the use of the gradient of the log-law to determine U_τ. Some of the methods used to obtain an estimate of U_τ over rough walls are the von Kármán-momentum-integral equation, presure-tapped roughness elements (see Perry, Schofield & Joubert 1969) and a drag balance. The momentum-integral method is known to be highly sensitive to any three-dimensionality of the flow and the determination of the derivatives of the various mean-flow quantities from a few experimental data points is a highly inaccurate process. The pressure tapping of roughness elements is only practical with large elements. The drag-balance method gives reasonable results but the technique requires considerable development and care to minimize or account for gap leakage. A method was developed here to determine the wall shear velocity U_τ and the error in origin e, that relies on the universality of the velocity-defect law. This method is similar to the 'wake alignment' method used by Perry & Joubert (1963) and is described below.

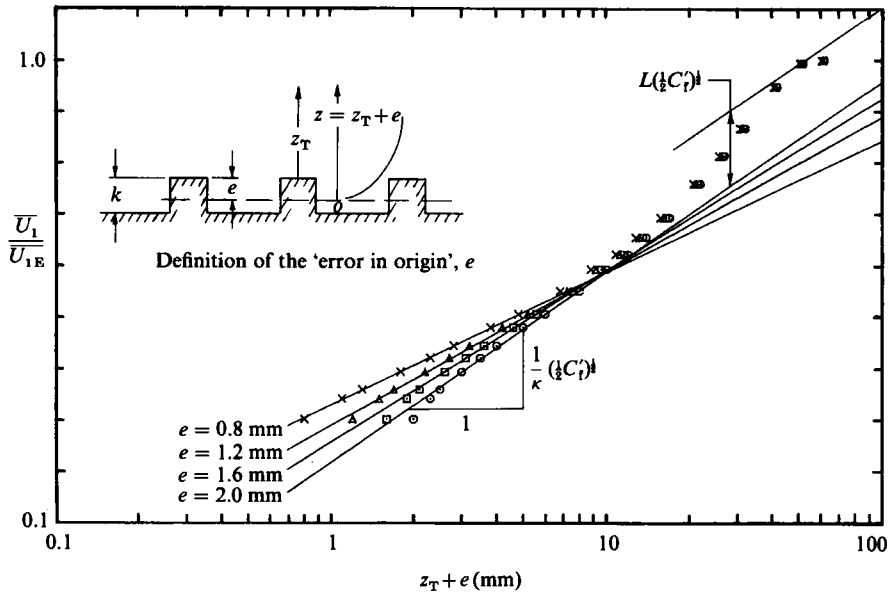

FIGURE 5. A Mean-velocity profile over the mesh roughness with different values of e.

2.3. *The velocity-defect-law method of determining C_f' and e*

The velocity-defect law is given by

$$\frac{\overline{U_{1E}} - \overline{U_1}}{U_\tau} = f(\xi), \tag{6}$$

where $\overline{U_{1E}}$ is the free-stream velocity, $\xi = z/\Delta_E$,

$$\Delta_E = \frac{\delta^*}{C_1}\left(\frac{2}{C_f'}\right)^{\frac{1}{2}}, \quad C_1 = \int_0^\infty f(\xi)\,d\xi,$$

C_f' is the local skin friction coefficient and δ^* is the displacement thickness. Hama (1954) defined $f(\xi)$ for a zero-pressure-gradient boundary layer to be

$$f(\xi) = -\frac{1}{\kappa}\ln(\xi) + 2.309 \quad (0 \leqslant \xi \leqslant 0.15), \tag{7a}$$

$$= 9.6(1-\xi)^2 \quad (0.15 \leqslant \xi \leqslant 1). \tag{7b}$$

Using 7(*a*) and (*b*) the constant C_1 has a value of 3.3715.

Figure 5 shows a typical mean-velocity profile measured over a rough surface plotted as $\overline{U_1}/\overline{U_{1E}}$ *vs.* $\log(z_T + e)$ for different values of e, where z_T is the wall distance measured from the tops of the roughness elements and e is the error in origin, i.e. $z = z_T + e$. For each value of e, a straight line is fitted to the log-law region and this has a slope of $(1/\kappa)(\frac{1}{2}C_f')^{\frac{1}{2}}$ and the maximum deviation of the wake from this line has a value of $L(\frac{1}{2}C_f')^{\frac{1}{2}}$. Cross-plots of e *vs.* L (figure 6*a*) and e *vs.* $(\frac{1}{2}C_f')^{\frac{1}{2}}$ (figure 6*b*) are made. According to the Hama velocity-defect law, e and $\frac{1}{2}(C_f')^{\frac{1}{2}}$ have the correct value when $L = 2.489$.†

† In previous publications of this work an *incorrect* value of $L = 2.56$ was given. The error in the estimates of C_f' and e caused by this were negligible.

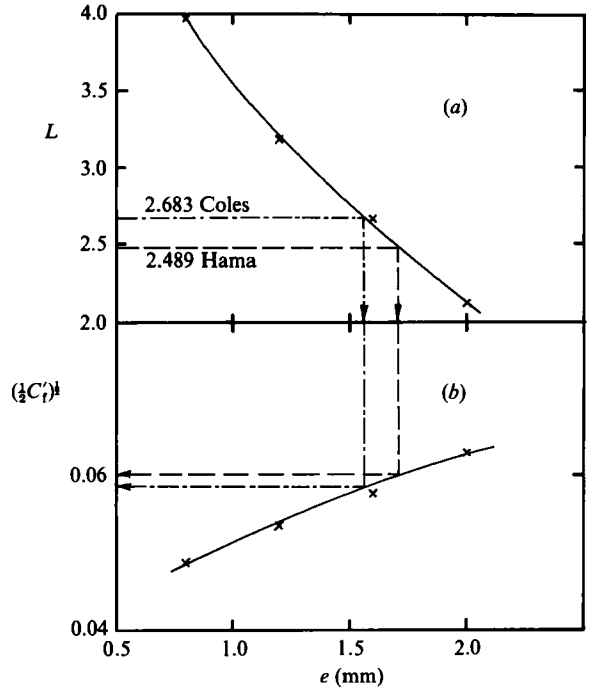

FIGURE 6. Method of obtaining e and $(\frac{1}{2}C_f')^{\frac{1}{2}}$ using the velocity-defect-law method (Hama 1954 and Coles 1968).

Alternatively, Coles' (1968) law of the wake could have been used to formulate $f(\xi)$ with a Coles wake parameter of 0.55 and this gives values of $L = 2.683$ and $C_1 = 3.780$. This changes the estimates of C_f' and e slightly. Throughout this paper the Hama formulation has been used to determine the lengthscale Δ_E.

On rough surfaces, it has been known for some time that the Reynolds shear stress measured with X-wires falls off as the wall is approached. This fall-off cannot be explained in terms of viscous stresses. As pointed out by Perry *et al.* (1969) this implies that a stationary mean flow 'wave', which transports momentum, might exist above the roughness elements.

3. An investigation of Reynolds shear stress over rough and over smooth surfaces

3.1. *The wavy wall*

Mean-velocity profiles measured over the wavy wall were of an unusual shape, no logarithmic region existed and close to the wall the gradient of mean velocity $(\mathrm{d}\overline{U_1}/\mathrm{d}z)$ was slightly negative. Thus the velocity-defect-law method could not be used to obtain estimates of U_τ and e. This odd profile is thought to be because k/δ_{99} is large, i.e. due to a lack of development length.

Figure 7 defines the various relevant quantities for flow over the wavy wall. The instantaneous velocities for a given z are

$$U_1(x,t) = \langle \overline{U_1} \rangle + \overline{u_1(x)} + u_1(x,t), \tag{8}$$

where

$$\langle (\,) \rangle = \frac{1}{\lambda} \int_x^{x+\lambda} (\,)\,\mathrm{d}x, \tag{9}$$

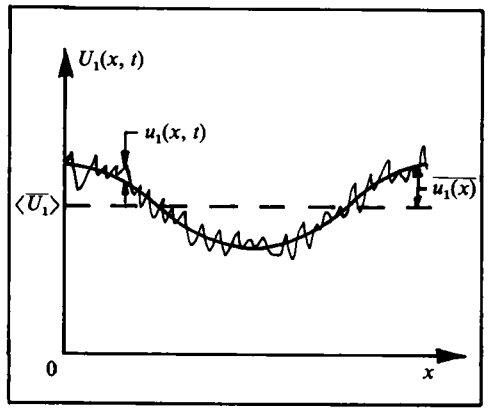

FIGURE 7. Definition of flow quantities over the wavy wall.

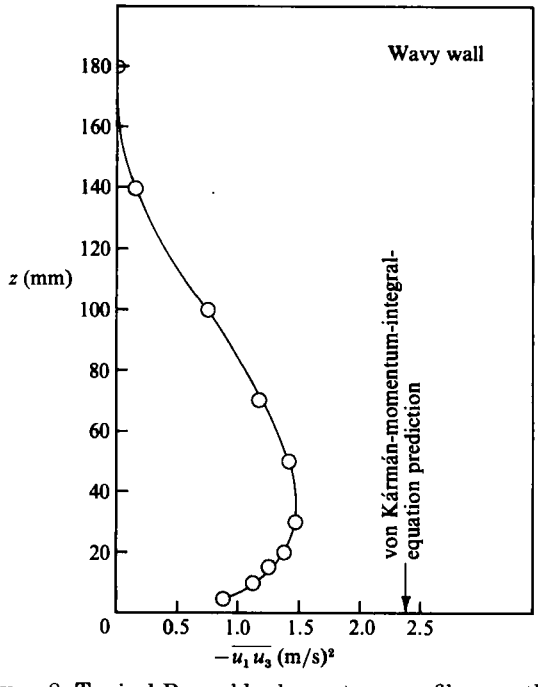

FIGURE 8. Typical Reynolds-shear-stress profile over the wavy wall.

and by definition
$$\frac{1}{\lambda}\int_x^{x+\lambda} \overline{u_1(x)}\,\mathrm{d}x = 0, \tag{10}$$

note that the symbols $\langle\ \rangle$ denote spatial averaging over one wavelength λ of the wavy surface (see (9) and figure 3). Similarly,

$$\frac{1}{\lambda}\int_x^{x+\lambda} \overline{u_3(x)}\,\mathrm{d}x = 0, \tag{11}$$

and $\langle \overline{U_3} \rangle$ is taken to be zero close to the wall. Suppose we consider the case where the streamwise development of the boundary layer is very slow and pressure-gradient

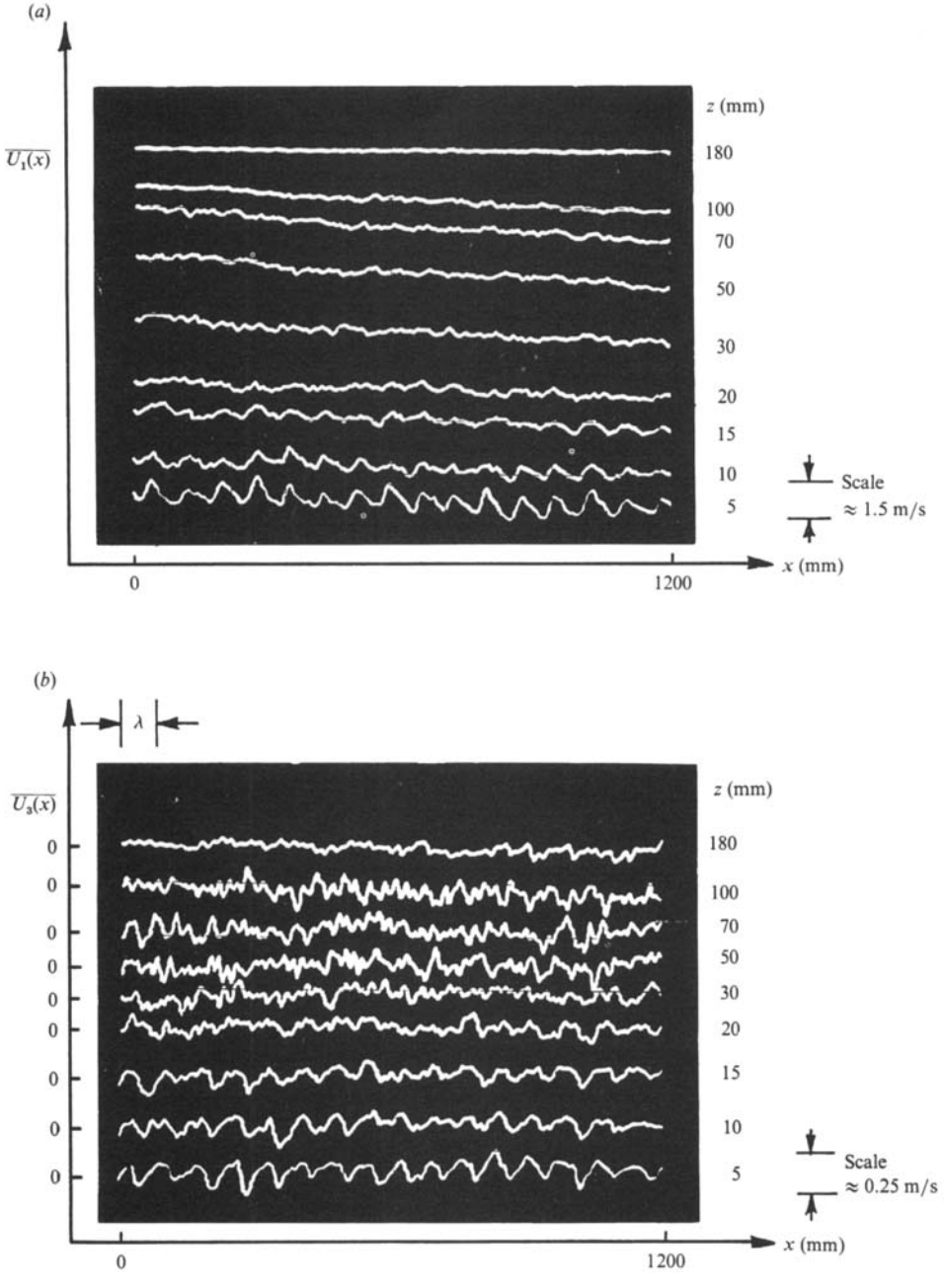

FIGURE 9. Plots of (*a*) $\overline{U_1(x)}$ and (*b*) $\overline{U_3(x)}$ above the wavy wall obtained with the flying hot-wire for varying values of z. Origins of $\overline{U_3(x)}$ have been shifted in (*b*).

effects are small, then for z_T sufficiently small the effective wall shear stress τ_0 is

$$\tau_0 = -\rho\langle\overline{u_1(x,t)\,u_3(x,t)}\rangle - \rho\langle\overline{u_1(x)}\,\overline{u_3(x)}\rangle, \tag{12}$$

where ρ is the fluid density. This will correspond to the mean force acting on the wall per unit area due to viscous and form drag on the roughness elements. For the rough

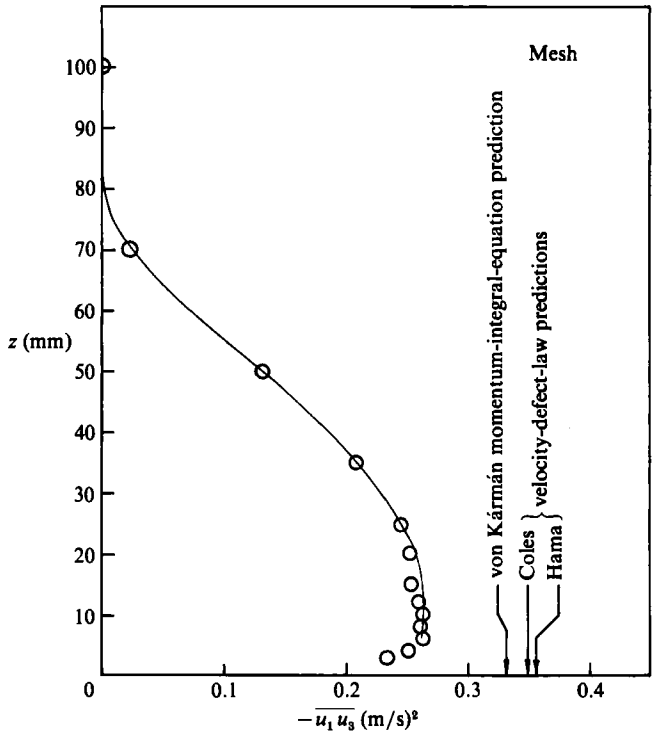

FIGURE 10. Typical Reynolds-stress profile over the mesh roughness, $x = 2500$ mm.

surfaces tested here $\overline{u_1(x,t)\,u_3(x,t)}$ was found to be invariant with x over a wavelength λ and so

$$\tau_0 = -\rho\langle\overline{u_1(t)\,u_2(t)}\rangle - \rho\langle\overline{u_1(x)}\,\overline{u_3(x)}\rangle. \tag{13}$$

The first term is the Reynolds shear stress that would be seen by a stationary probe and the second represents the contribution to the momentum transport by a stationary wave above the elements. Figure 8 shows a Reynolds-shear-stress profile measured over the wavy wall with a stationary X-wire. As can be seen the Reynolds shear stress falls off towards the wall and the shear stress is not even close to the value obtained using the momentum integral equation. Figure 9 shows plots of $\overline{U_1}(x)$ and $\overline{U_3}(x)$ measured over the wavy wall by the flying hot wire at different distances from the wall. It can be seen that the variations in $\overline{U_1(x)}$ and $\overline{U_3(x)}$ are significant but attenuate away from the wall and that they are approximately 90° out of phase. Because of this phase difference, the spatially averaged quantity $\langle\overline{u_1(x)}\,\overline{u_3(x)}\rangle$, which represents the contribution by a stationary wave, was negligible. Spanwise traverses of $\overline{U_2}$ showed that secondary flow in the tunnel was very small.

3.2. *The mesh roughness*

Mean-velocity profiles measured over the mesh roughness showed that the velocity-defect-law method could be applied to determine the value of U_τ as the values agreed reasonably with the values determined using the momentum integral equation. However, neither of these values agreed with the value determined from the X-wire Reynolds-shear-stress profile shown in figure 10 (which falls off as the wall is approached instead of asymptoting to a constant value as would be expected for

constant pressure layers). It was felt that inadequate spatial resolution of the X-wires may have been the cause but repeating the test with a set of X-wires with etched lengths reduced from 1.2 to 0.5 mm and with spacing between the wires reduced from 1.0 to 0.5 mm gave the same result.

The dynamic calibration facility enabled the calibrated X-wires to be given a known Reynolds shear stress by oscillating the wires in a uniform flow with known sinusoidal velocity perturbations u_1 and u_3 and with a known phase difference. This could be compared with the measured X-wire Reynolds shear stress and agreement was found to be within 1 %.

It was therefore decided to measure the Reynolds shear stress over a smooth plate as the Clauser-chart method could be used as another independent method of determining U_τ. The X-wire Reynolds shear stress over a smooth wall gave the same wall shear velocity as the Clauser-chart method and the shape of the profile was also correct (i.e. no fall-off as the wall is approached). This confirmed that the X-wires, anemometers, calibration and sampling techniques were operating correctly. The tests on the mesh roughness were repeated with a 'smooth-wall check' immediately after calibration as follows. A smooth plate was placed over the mesh roughness, a mean velocity profile was measured and the wall shear stress determined using a Clauser chart. After calibrating the X-wires, the calibration was checked by measuring the Reynolds shear stress over the smooth plate, and having determined that the X-wires were giving the correct value of Reynolds shear stress, the smooth plate was immediately removed uncovering the mesh roughness. The Reynolds-shear-stress profile obtained over the mesh roughness was the same 'incorrect' profile as obtained before. As the shear stress determined using the velocity-defect-law method seemed to give reasonable agreement with a momentum balance, it was suspected that for some reason the X-wires were unable to determine the correct value of $-\overline{u_1 u_3}$ over a rough surface.

3.3. *Resolution of the mystery*

In view of the above, a reason was sought for the misbehaviour of the X-wires in measuring the Reynolds shear stress above a rough surface. Tutu & Chevray (1975), Willmarth & Bogar (1977) and Kawal, Shokr & Keffer (1983) have shown that the use of X-wires in regions of very high turbulence intensity can result in large errors in measurement. Tutu & Chevray showed this by turbulence measurements in a turbulent jet and Willmarth & Bogar by turbulence measurements very close to a smooth wall. These large errors were due to the large angles made by the velocity vectors as they approached the X-wires. One of the major differences between flow over a smooth surface and that over a rough surface is that for a given $\Delta_E U_\tau/\nu$, $\overline{U_1}/U_\tau$ at a given z/Δ_E has a much lower value on a rough surface. In fact,

$$\left(\frac{\overline{U_1}}{U_\tau}\right)_R = \left(\frac{\overline{U_1}}{U_\tau}\right)_S - \frac{\Delta U}{U_\tau}, \tag{14}$$

where $\Delta U/U_\tau$ is the Hama (1954) roughness function; the suffix R signifies a rough surface and the suffix S signifies a smooth surface. From the theory given earlier it would be expected that in the turbulent wall region $\overline{u_3^2}/U_\tau^2 = A_3$ for z_+ sufficiently large. Hence in this region $\overline{u_3^2}$ scales with U_τ^2. Since $\overline{U_1}/U_\tau$ for a rough wall is less than that for a smooth wall, it stands to reason that the instantaneous velocity vectors approaching the X-wires in the plane of the wires will be undergoing a larger change in angle over the rough wall. One could imagine that all velocity vectors approaching the probe are contained in an elliptical cone and the cone angle above a rough surface

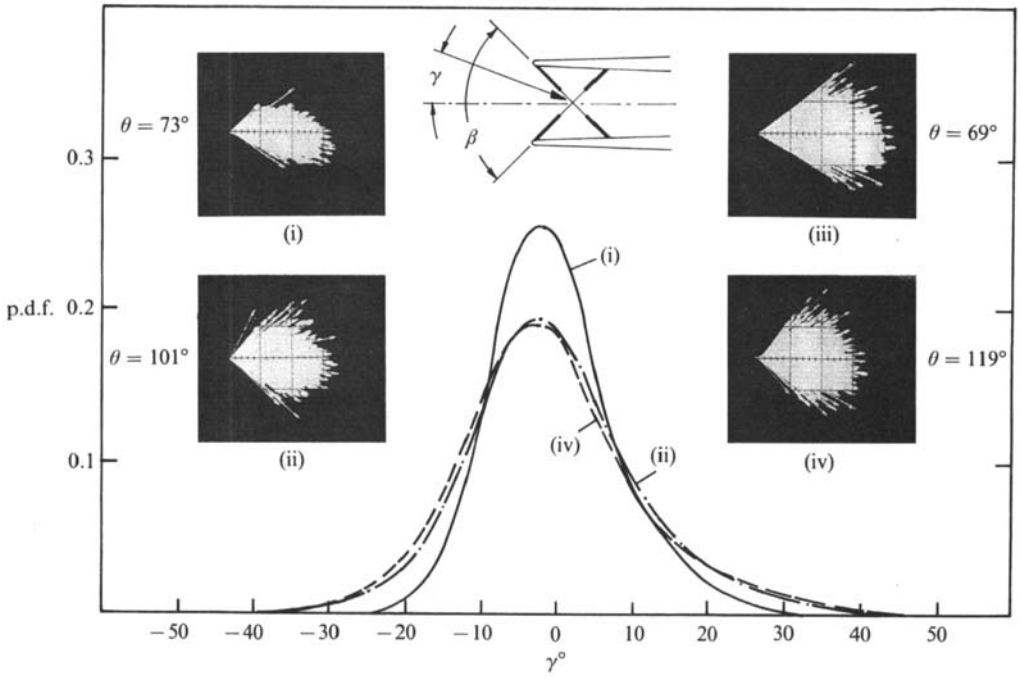

FIGURE 11. p.d.f. of γ and velocity-vector diagrams over the mesh roughness for the following cases: (i) ——, $\beta = 90°$ stationary wire, vectors relative to the wall; (ii) –·–·–, $\beta = 120°$ stationary wire, vectors relative to the wall; (iii), $\beta = 120°$ flying wire, vectors relative to the *probe*; (iv) – – –, $\beta = 120°$ flying wire, vectors relative to the wall. For all cases, $z = 5$ mm, $\overline{U_{1E}} = 10$ m/s, $\overline{U_1} = 4.0$ m/s, $x = 2500$ mm, and for cases (iii) and (iv) the bias velocity was 2.5 m/s.

will exceed that on a smooth surface. We shall define θ as the maximum inferred cone angle of the velocity vectors measured in the plane of the X-wires (i.e. (x, z)-plane for $-\overline{u_1 u_3}$ measurements), γ as the instantaneous velocity vector angle and β as the included angle of the X-wires (see figure 11). It is obvious that if γ approaches or exceeds β then any measurements taken with such a set of X-wires would be completely erroneous.

Inserts (i) and (ii) in figure 11 show plots of the velocity vectors measured with $\beta = 90°$ and $\beta = 120°$ wires when placed close to the mesh roughness. The $\beta = 90°$ wires measured a cone angle θ of 73° whereas the $\beta = 120°$ wires measured a cone angle of 101°. It was found by perturbing the wires with a known Reynolds shear stress that the Reynolds shear stress measured by the $\beta = 90°$ wires deviated from ideal behaviour at a known θ of 20°, whereas the $\beta = 120°$ wires deviated at 55° for the calibration technique used here (see Lim 1985). This would suggest that the cone angles in the flow are still too large to be adequately resolved by the $\beta = 120°$ wires. The $\beta = 120°$ X-wire Reynolds shear stress was higher than those indicated by the $\beta = 90°$ wires but still fell short of the value predicted by the velocity-defect-law method and the von Kármán-momentum-integral method. It was then decided to attempt to measure the Reynolds shear stress using the flying hot wire. Flying the X-wires would have the following advantages:

(i) It would reduce the velocity-vector cone angles seen by the X-wires by imposing an additionional $\overline{U_1}/U_\tau$ of about 2.5;

(ii) The effect of u_2 would be reduced;

(iii) The contribution of the stationary wave could be determined.

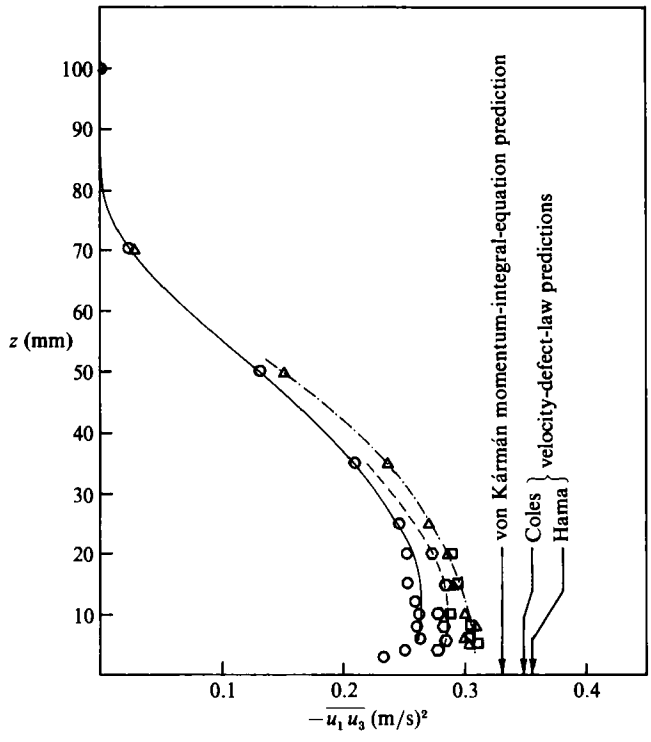

FIGURE 12. Reynolds-shear-stress profiles over the mesh roughness, $x = 2500$ mm. ○, $\beta = 90°$ stationary; ○, $\beta = 90°$ flying; □, $\beta = 120°$ flying; △, $\beta = 120°$ stationary.

Figure 12 shows the Reynolds shear stress measured by flying the $\beta = 90°$ and $\beta = 120°$ wires and also earlier profiles measured with stationary wires so a comparison can be made between the different methods. The difference in Reynolds shear stress at the wall can be clearly seen. However, note that the values obtained with the $\beta = 120°$ wires seem to be independent of bias velocity and this would seem to indicate that the $\beta = 120°$ stationary X-wires are not being affected by excessive velocity-vector cone angles over the mesh roughness. The effect of the stationary wave over the mesh roughness was found to be negligible. Insert (iii) in figure 11 shows velocity-vector cone angles seen by the $\beta = 120°$ wires as they are being 'flown' at a bias velocity of $\overline{U_1}/U_\tau = 2.5$. Note how the cone angle θ decreases from 101° to 69° as $\overline{U_1}/U_\tau$ is increased from 4.0 to 6.5. Insert (iv) in figure 11 shows the same data with the bias velocity of the sled subtracted and the cone angle θ is 119°. Thus the inferred cone angle for the stationary $\beta = 90°$ wires is incorrect if the $\beta = 120°$ wire results are taken to be correct.

Some normalized p.d.f.s of γ are also shown in figure 11 for the various cases. Note how the $\beta = 120°$ wires gave similar p.d.f.s for the velocity vectors relative to the wall whether the measurements were made with flying or stationary wires. From the fact that both cases also gave similar Reynolds shear stress profiles, we concluded that the $\beta = 120°$ wires were giving the correct readings whether stationary or flying.

It is thought that the value of U_τ inferred from the $\beta = 120°$ wire Reynolds shear stress profiles is correct and that the velocity-defect-law method is inaccurate because of insufficient flow development. The velocity-defect-law method uses the size of the wake and this has been shown to depend on flow development (see Coles 1962). It

is thought that the flow has not yet reached its asymptotic state where this law would be valid.

The $\beta = 90°$ and $\beta = 120°$ stationary wires both gave identical Reynolds shear stress profiles and similar instantaneous velocity-vector angle p.d.f.s over the smooth wall, where $\overline{U_1}/U_\tau \approx 20$. The cone angle measured with the $\beta = 120°$ wires was 30°.

Of course there will be an even larger spread in vector angles in the (x, y)-plane. Analysis shows that the resulting cross-contamination from the u_2 component to $-\overline{u_1 u_3}$ is small since u_2 is uncorrelated with u_1 and u_2. However, the other turbulence intensity measurements ($\overline{u_2^2}$ and $\overline{u_3^2}$) may be influenced by this cross-contamination.

The work of Perry *et al.* (1983), which contains preliminary findings of the work reported here, led Acharya & Escudier (1984) to conduct a separate set of experiments over a similar 'mesh' type roughness. They used $\beta = 90°$ and $\beta = 120°$ stationary wires together with a floating-element drag balance and assumed linearity about the hot-wire anemometer operating point when reducing their data. Their findings are in general agreement with the work reported here. However, the differences in $-\overline{u_1 u_3}$ they measured using a $\beta = 90°$ and a $\beta = 120°$ wire were not as large as those reported here.

4. Turbulence intensity and spectral results over the smooth wall and the mesh roughness

Mean flow, broadband turbulence intensity and spectral measurements were taken over a smooth wall at six values of K_τ in a nominally zero pressure gradient, where $K_\tau = \Delta_E U_\tau/\nu$, the von Kármán number. The cases measured are shown in table 1. Measurements were also taken over the mesh roughness in a zero pressure gradient at four values of K_τ, and these are given in table 2. Here, x is measured from the trip wire and θ is the momentum thickness. Unless otherwise stated all u_2- and u_3-results were measured with a stationary $\beta = 90°$ X-wire and the u_1-results with a stationary normal wire.

4.1. *Smooth-wall spectra – turbulent wall region*

All smooth-wall spectra shown here are for the turbulent wall region, tentatively defined as $z_+ > 100$; $z/\Delta_E < 0.15$. Figure 13 (*a*, *b*) shows the u_1-spectra scaled with inner-flow and outer-flow scaling respectively. These spectra seem to follow the scheme suggested in figure 1 (*a*, *b*) reasonably well. An inverse-power-law region, (2), can be seen in both figures and an inertial subrange (3) in figure 13 (*a*). If a plot was to be made of $\log(k_1 z)_p$ *vs.* $\log(z_+)$, the expected slope of the line will be $+\frac{3}{4}$ (see §1). Perry *et al.* (1986) showed that if hot-wire spatial resolution is a problem in this wavenumber region, the slope of the line will be $+1$. Figure 14 shows plots of $\log(k_1 z)_p$ *vs.* $\log(z_+)$ determined from the experimental u_1-, u_2- and u_3-spectra. The slope of $+\frac{3}{4}$ for the u_1-case shows that spatial resolution at wavenumbers up to the end of the inertial subrange is not a problem at least for the normal wires used here. Figure 15 (*a*) shows the u_2-spectra scaled with inner-flow scaling coordinates. The u_2-spectra can be seen to follow the same scaling laws as the u_1-spectra. The inertial subrange is shorter in the u_2-spectra and this is probably caused by premature peel-off of the spectra caused by a spatial-resolution problem confirmed in figure 14. Figure 15 (*b*) shows the u_2-spectra with outer-flow scaling and these appear to follow the scaling scheme shown in figure 1 (*b*). The u_1- and u_2-spectra should collapse at low wavenumbers with outer-flow scaling, but a considerable degree of scatter at low wavenumbers can be seen in figures 13 (*b*) and 15 (*b*). This is thought to be due to the

x (mm)	$\overline{U_{1E}}$ (m/s)	K_τ	Δ_E (mm)	$R_\theta (= U_{1E}\theta/\nu)$
500	10	522	17	1200
1750	10	1163	43	2790
3000	10	1751	69	4240
500	30	2164	29	5110
1750	30	3502	49	8660
3000	30	4787	68	12060

TABLE 1. Smooth-wall flow parameters

x (mm)	$\overline{U_{1E}}$ (m/s)	K_τ	Δ_E (mm)	R_θ
600	10	1413	36	2730
2500	10	3484	96	7280
600	20	2957	37	5560
2500	20	6841	95	14120

TABLE 2. Mesh roughness flow parameters

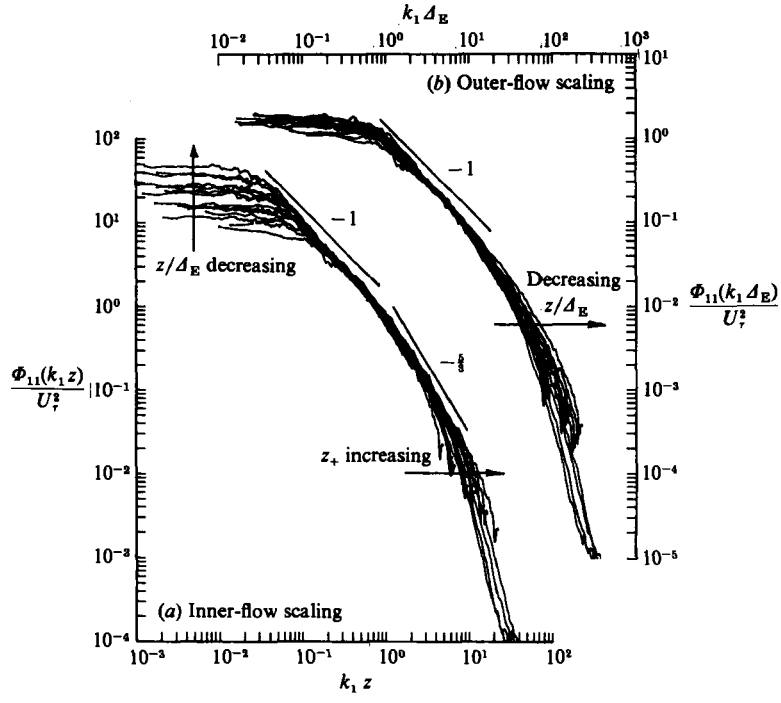

FIGURE 13. u_1-spectra for varying values of z/Δ_E in the turbulent wall region over the smooth wall for values of K_τ given in table 1. (*a*) inner-flow scaling; (*b*) outer-flow scaling.

fact that the application of Taylor's (1938) hypothesis of frozen turbulence may lead to errors in inferred wavenumber, as eddies of different scale have different convection velocities (see Wills 1964; Perry *et al.* 1986). Perry & Abell (1977) showed that an error in the inferred wavenumber does not affect the collapse of the data to an inverse-power-law region since such an error shifts spectra plotted on logarithmic axes along a line of slope -1.

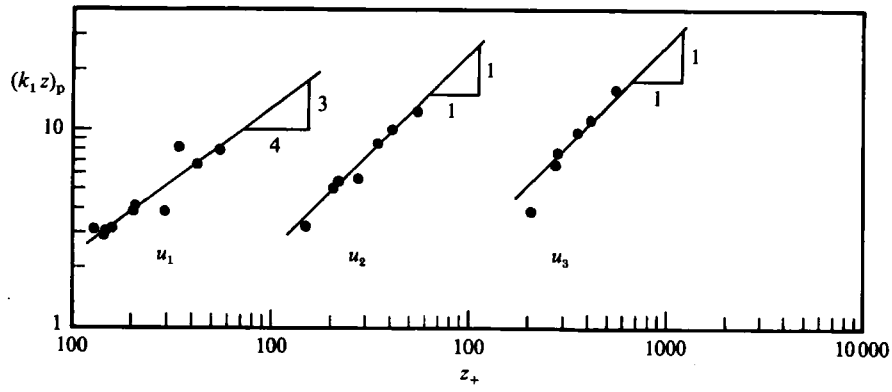

FIGURE 14. Plots of $(k_1 z)_p$ *vs.* z_+ determined from the smooth u_1-, u_2- and u_3-spectra measured in the turbulent wall region.

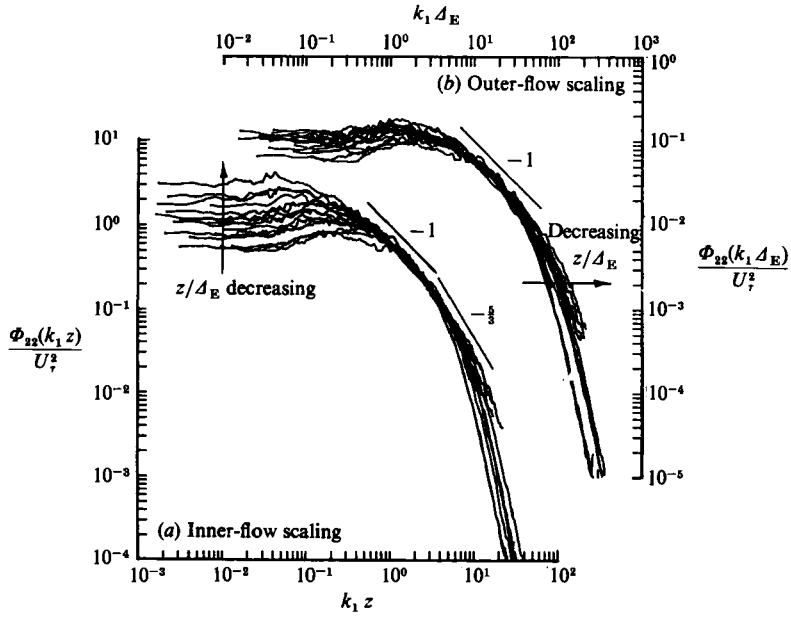

FIGURE 15. u_2-spectra for varying values of z/Δ_E in the turbulent wall region over the smooth wall for varying values of K_τ given in table 1. (*a*) inner-flow scaling; (*b*) outer-flow scaling.

Figure 16 shows the u_3-spectra plotted with inner-flow scaling. These spectra do not collapse as expected (figure 2) but there are two encouraging features of this plot. Firstly, there is no inverse power law region and secondly, the low wavenumber peel-offs do not depend on z/Δ_E. The lack of collapse at low wavenumbers cannot be blamed on the spread in convection velocities as only eddies of scale of order z contribute significantly to $\overline{u_3^2}$ at z. Instead, this is thought to be due to a cross-contamination problem, where the matched X-wire signals are being influenced by the velocity component normal to the plane of the wires. This may be caused by misalignment of the hot-wire filaments relative to the plane of measurement, either due to the plane of the wires not being parallel to each other or normal to the wall, or bowing of the hot-wire filaments. Since $\overline{u_3^2}$ is significantly smaller than $\overline{u_1^2}$ and $\overline{u_2^2}$,

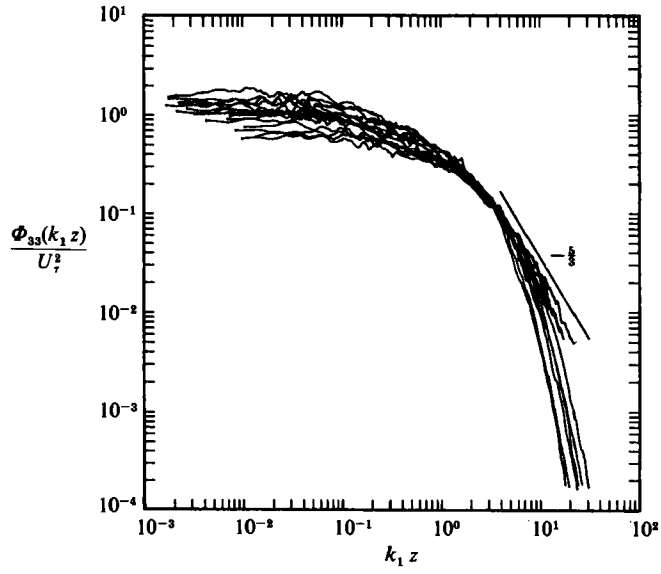

FIGURE 16. u_3-spectra for varying values of z/Δ_E in the turbulent wall region over the smooth wall with inner-flow scaling for different values of K_τ given in table 1.

the $\overline{u_3^2}$ measurements would suffer from a larger fractional error owing to cross-contamination. The inertial subrange is short because of the spatial-resolution problem which is confirmed in figure 14.

4.2. *Mesh spectra – turbulent wall region*

For the mesh roughnesss, the turbulent wall region is tentatively defined as $2k < z < 0.15\Delta_E$, where the roughness height k is 1.5 mm. Figure 17 (a, b) shows the mesh roughness u_1-spectra plotted with inner-flow and outer-flow scaling respectively. These rough-wall spectra appear to follow the same scaling laws as the smooth-wall spectra shown in figure 13 (a, b).

Because the scale of the smallest hierarchy on a rough surface is thought to scale with k, the total number of hierarchies over any given roughness geometry should depend on Δ_E/k alone. At a fixed z/Δ_E, z_+ is larger over a rough wall than a smooth wall, leading to a longer inertial subrange in the rough-wall spectra. The measured spectra show this to be the case. Figure 18 shows a plot of $\log(k_1 z)_p$ *vs.* $\log(z_+)$ and this verifies that the normal wire used had adequate spatial resolution.

Figure 19 (a, b) shows the mesh roughness u_2-spectra plotted with inner-flow and outer-flow scaling respectively. The u_2-spectra appear to follow the same scaling laws as the corresponding u_1-spectra. However, the collapse onto an inverse-power-law region is not as convincing as in the case of the u_1-spectra. On a smooth wall the lower limit of z/Δ_E in the turbulent wall region is much smaller than that on the mesh roughness for the measurements presented here, and since the number of observed hierarchies depends on z/Δ_E, the length of the inverse-power-law region should be shorter in the rough-wall spectra and this is confirmed in figures 17 and 19. These X-wires also had a spatial-resolution problem, as can be seen in figure 18. The collapse of the rough-wall u_1- and u_2-spectra at low wavenumbers plotted with outer-flow scaling is not as good as over the smooth surface and this can again be attributed to the error in inferred wavenumber due to the use of Taylor's hypothesis. Because

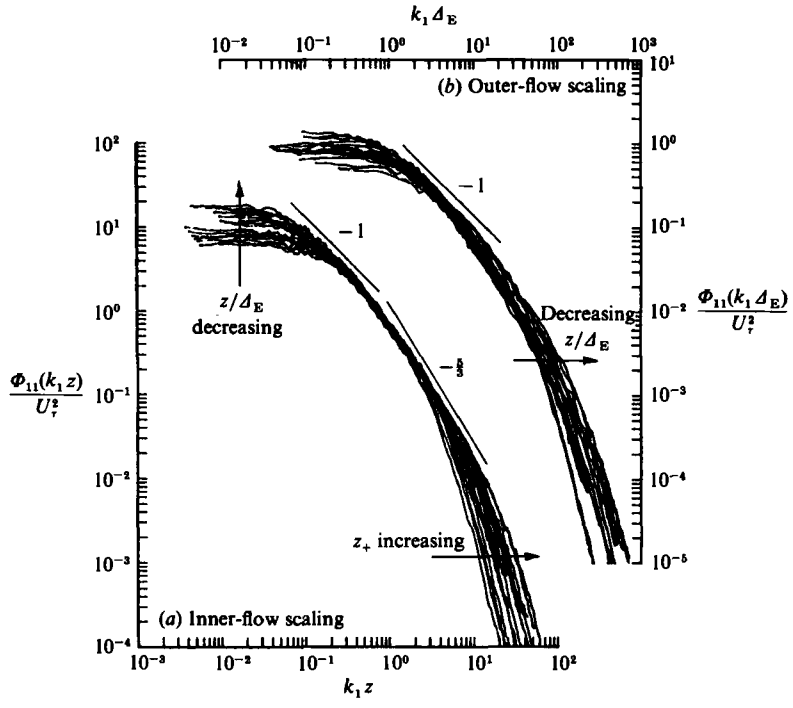

FIGURE 17. u_1-spectra for varying values of z/Δ_E in the turbulent wall region over the mesh roughness for values of K_τ given in table 2. (*a*) inner-flow scaling; (*b*) outer-flow scaling. ($\beta = 120°$ stationary X-wire U_τ).

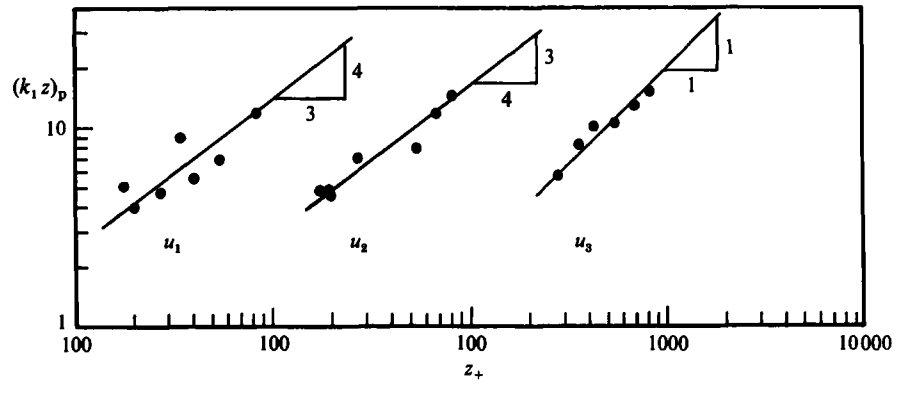

FIGURE 18. Plots of $(k_1 z)_p$ *vs.* z_+ determined from the mesh roughness u_1-, u_2- and u_3-spectra measured in the turbulent wall region.

the roughness causes a decrement in $\overline{U_1}/U_\tau$ equal to $\Delta U/U_\tau$, (the roughness function), the fractional spread in convection velocity between eddy scales will be higher and hence the error in inferred wavenumber over a rough surface is greater than over a smooth surface (see Perry & Abell 1977).

Figure 20(*a*, *b*) shows the u_3-spectra plotted with inner- and outer-flow scaling respectively. A short inertial subrange is present. No collapse is expected with outer-flow scaling and this is the case.

The u_2- and u_3-spectra over the mesh roughness were measured before the

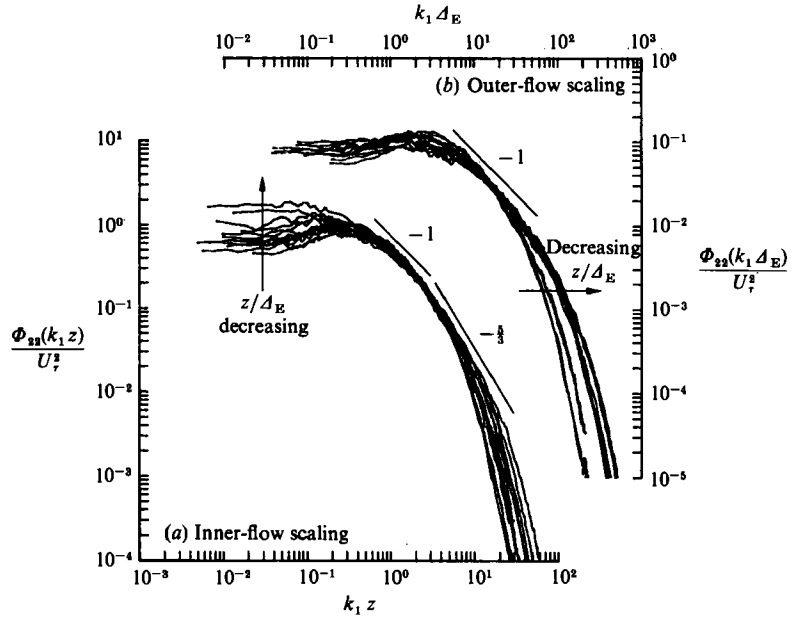

FIGURE 19. u_2-spectra for varying values of z/Δ_E in the turbulent wall region over the mesh roughness for values of K_τ given in table 2. (*a*) inner-flow scaling; (*b*) outer-flow scaling. ($\beta = 120°$ stationary X-wire U_τ).

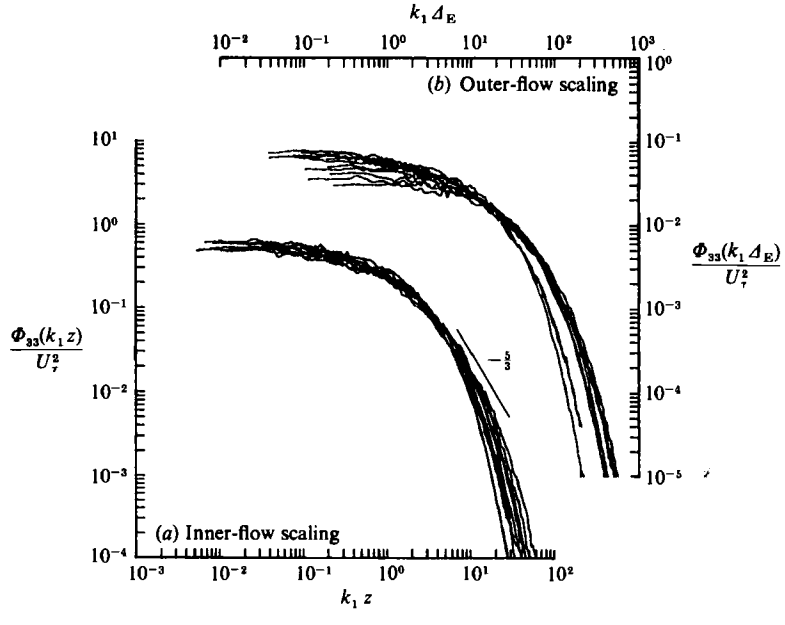

FIGURE 20. u_3-spectra for varying values of z/Δ_E in the turbulent wall region over the mesh roughness for values of K_τ given in table 2. (*a*) inner-flow scaling; (*b*) outer-flow scaling. ($\beta = 120°$ stationary X-wire U_τ).

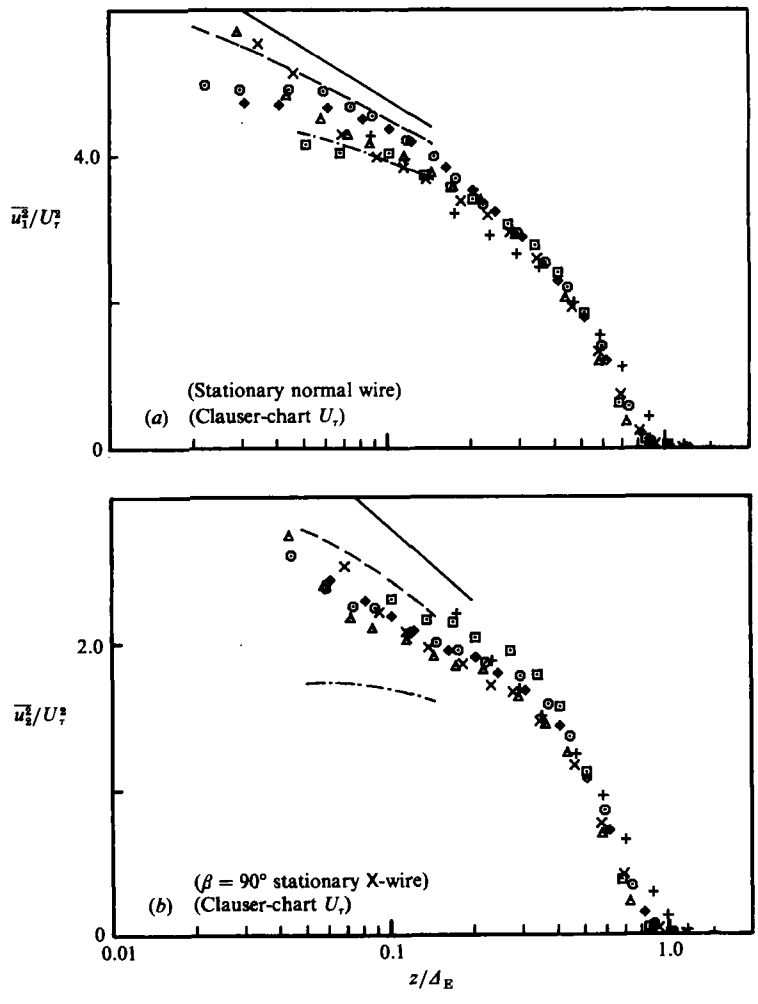

FIGURE 21. Turbulence intensity distributions of (*a*) $\overline{u_1^2}/U_\tau^2$ and (*b*) $\overline{u_2^2}/U_\tau^2$ over the smooth wall, K_τ: +, 522; ×, 1163; △, 1751; □, 2164; ◇, 3502; ⊙, 4787. Predicted distributions (equation (4) for $\overline{u_1^2}/U_\tau^2$ and a similar equation for $\overline{u_2^2}/U_\tau^2$ using the constants given in table 3) for K_τ: ——, $\to\infty$; –·–·–, 522; – – – –, 4787.

cone-angle problem was discovered and were unfortunately measured with $\beta = 90°$ wires. Since a cone-angle problem is known to exist some doubt must be placed on the accuracy of these results. In the next section we show that the use of $\beta = 120°$ wires is not sufficient to solve the cone-angle problem for $\overline{u_3^2}$ measurements and $\overline{u_2^2}$ measurements. One solution mght be to fly the wires for these measurements. Such a major undertaking has not yet been carried out. We believe that although the results are inaccurate they at least show qualitative support for the similarity proposals.

4.3. *Broadband turbulence intensities – smooth wall*

Figure 21 (*a*, *b*) shows the measured $\overline{u_1^2}$ and $\overline{u_2^2}$ distributions over the smooth plate and superimposed are the predicted distributions (equation (4) for $\overline{u_1^2}/U_\tau^2$ and a similar equation for $\overline{u_2^2}/U_\tau^2$ using the smooth-wall numerical constants given in table 3, which

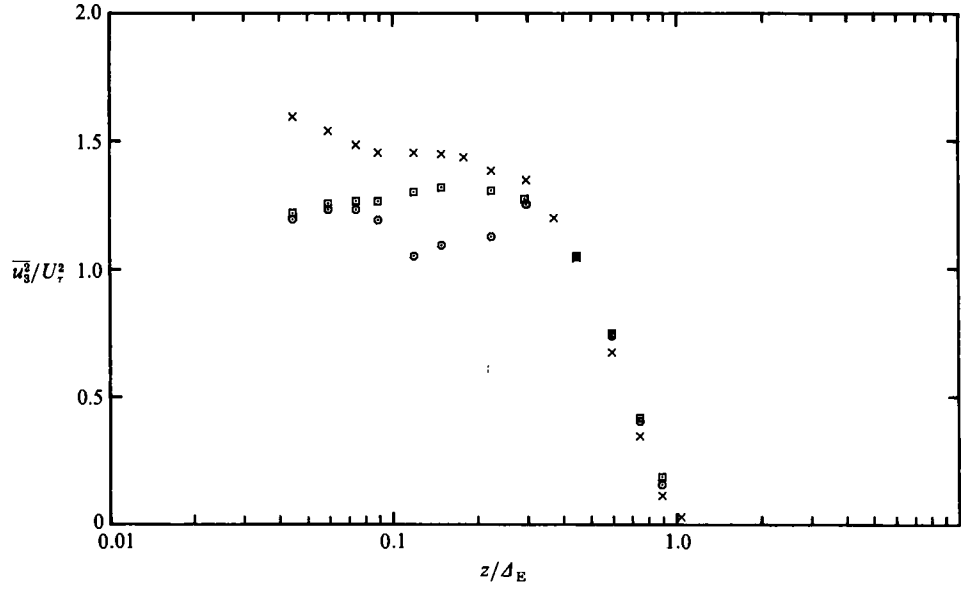

FIGURE 22. $\overline{u_3^2}/U_\tau^2$ distributions over the smooth wall measured with three different X-wires. $K_\tau = 4787$. $\beta = 90°$ stationary X-wire; Clauser-chart U_τ. ×, cross-contamination from u_2 and u_1 suspected; ⊙, bowed wires; ⊡, wires with no obvious defects; All three X-wires gave the same correct value of $-\overline{u_1 u_3}$ and values of $\overline{u_1^2}$ that agreed with those obtained with a normal wire.

were determined from spectra). The measured distributions seem to behave as the theory predicts especially in the u_1-case, where a normal wire (which is less prone to error compared with a X-wire) was used in the measurements.

As indicated earlier, we were suspicious of the u_3 measurements and decided to repeat the measurements with many different wires at the highest value of K_τ. The results of three of these X-wires are shown in figure 22. Two of the wires represent the extreme and one the norm. All three wires ($\beta = 90°$) gave Reynolds shear stresses which when extrapolated to the wall agreed closely with the Clauser-chart result. They also gave the same values of $\overline{u_1^2}$ as given by a normal wire to within 5 % in energy. These results indicate the difficulty in obtaining consistency in the $\overline{u_3^2}$ results. With the $\beta = 120°$ wires the inferred values of $\overline{u_3^2}/U_\tau^2$ were even more erratic from one set of wires to another. This was later experienced by Acharya & Escudier (1984) who measured $\overline{u_3^2}/U_\tau^2$ with $\beta = 90°$ and $\beta = 120°$ wires above a rough surface and in a smooth-walled pipe. Cross-contamination of velocity components is the most likely cause, since there is an even larger spread in vector angles in the (x, y)-plane, the effects of which are yet to be investigated. It was therefore decided to see what values of $\overline{u_3^2}/U_\tau^2$ other workers obtained in the turbulent wall region. We decided to plot $\overline{u_3^2}/U_\tau^2$ at $z/\Delta_E = 0.1$ *vs.* $\Delta_E U_\tau/\nu\,(= K_\tau)$ provided $zU_\tau/\nu > 100$ from all possible sources where the appropriate quantities were quoted or could be determined. Superimposed on this plot (figure 23) is (5) with $z/\Delta_E = 0.1$ for $A_3 = 1.0$, 1.5 and 2.0 and $C = 6.08$. This figure includes data from fully developed pipe and duct flow where Δ_E is taken as the pipe radius or duct half-width. It can be seen that there are considerable discrepancies between various workers even if we only consider in turn the boundary-layer results and the pipe and duct results. According to the Buckingham Π-theorem alone, smooth-wall boundary-layer results (assuming streamwise development is small) and smooth-pipe results should each collapse to

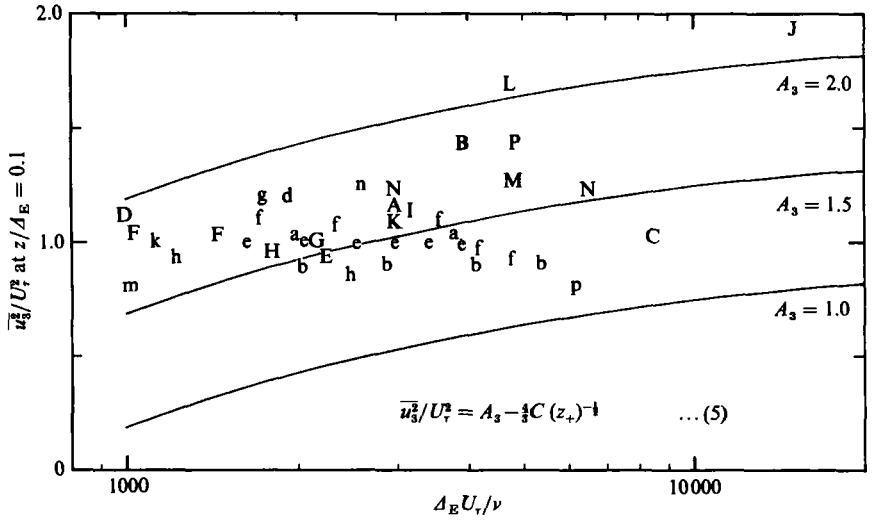

FIGURE 23. Normal turbulence intensity at $z/\Delta_E = 0.1$ versus von Kármán number for the data of various workers compared with equation (5) with $A_3 = 1.0$, 1.5 and 2.0 and $C = 6.08$.

Bounday layers

Acharya & Escudier (1984)	A	Rough wall
Andreopoulos & Bradshaw (1981)	B	Smooth wall
	C	Rough wall
Antonia & Luxton (1971)	D	Smooth wall
	E	Rough wall
Erm, Smits & Joubert (1986)	F	Smooth wall
Gupta & Kaplan (1972)	G	Smooth wall
Hancock & Bradshaw (1983)	H	Smooth wall
Klebanoff (1954)	I	Smooth wall
Mulhearn (1978)	J	Very rough wall
Murlis, Tsai & Bradshaw (1982)	K	Smooth wall
Willmarth & Bogar (1977)	L	Smooth wall
Present work	M	Smooth wall
	N	Rough wall
	P	Smooth wall, cross-contamination suspected

Pipes and ducts

Abell (1974)	a	Smooth pipe
	b	Rough pipe
Bremhorst & Walker (1973)	d	Smooth pipe
Henbest (1983)	e	Smooth pipe
	f	Rough pipe
Hooper & Harris (1982)	g	Smooth pipe
Hunt & Joubert (1979)	h	Smooth pipe
Laufer (1954)	k	Smooth pipe
Lawn (1971)	m	Smooth pipe
Sabot & Comte-Bellot (1976)	n	Smooth pipe
Sabot, Saleh & Comte-Bellot (1977)	p	Rough pipe

	A_1	A_2	A_3	B_1	B_2	C
Smooth	1.03	0.73	1.90	2.48	1.12	6.08
Rough	1.26	0.63	1.78	2.01	1.08	7.50

TABLE 3. Constants determined from experimental spectra

their own universal characteristic curve. It can be seen that this does not occur, thus strengthening the argument that this collection of results from various workers has errors. Furthermore, if the wall similarity and the attached eddy hypothesis outlined here are accepted all data including the rough-wall results should collapse on one universal curve irrespective of whether the data were derived from boundary-layer, pipe or duct flow. Because of the large amount of scatter between the results it is impossible to put a precise value on A_3. However, the majority of data suggest that A_3 has a value of about 1.5. The large variation in $\overline{u_3^2}/U_\tau^2$ between the results of the various workers is probably understandable in view of the results presented in figure 22.

4.4. *Broadband turbulence intensities – rough wall*

Figure 24(*a*) shows the $\overline{u_1^2}$ distribution measured over the rough wall, non-dimensionalized with the U_τ inferred from the Reynolds shear stress profiles ($\beta = 120°$ X-wires). Superimposed are the predicted distributions (4) for the turbulent wall region using the rough-wall constants given in table 3. Agreement is reasonable but it can be seen that the turbulence intensities seem to become constant as the wall is approached. A possible explanation may be that close to the wall $z < \delta_1$ and we are measuring below the lower limit of the turbulent wall region. In terms of Perry & Chong's model of wall turbulence, for $z < \delta_1$, where δ_1 is the scale of the smallest hierarchy, the turbulence intensity distribution falls below the logarithmic distribution (4) even for z_+ large.

Figure 24(*b*) shows the $\overline{u_2^2}$ distribution measured over the rough wall with the predicted distributions superimposed. The fit to the data is disappointing, probably due to inadequate spatial resolution and the presence of mean shear over the wires. Also $\beta = 90°$ wires were used.

Figure 24(*c*) shows the $\overline{u_3^2}$ distributions measured over the rough wall with $\beta = 90°$ wires. The cone-angle problem had not been discovered when these tests were carried out. The predicted distribution for $A_3 = 1.78$ (which was the value obtained from the rough-wall u_3-spectra) is superimposed. As mentioned earlier, $\overline{u_3^2}/U_\tau^2$ is not easy to measure accurately close to the wall, and over this surface, the cone-angle problem is present as well. However, figure 23 suggests that this data has $A_3 \approx 1.5$ and although this data is known to be inaccurate this seems to be in the correct region of the plot.

4.5. *Spectra in the fully turbulent region*

Following the extended Townsend-Reynolds-number similarity hypothesis (Perry & Abell 1977), the spectrum of the energy-containing components of u_i-velocity fluctuations in the fully turbulent region should follow

$$\frac{\Phi_{ii}(k_1 z)}{U_\tau^2} = F_{ii}(k_1 z, z/\Delta_{\mathrm{E}}). \tag{15}$$

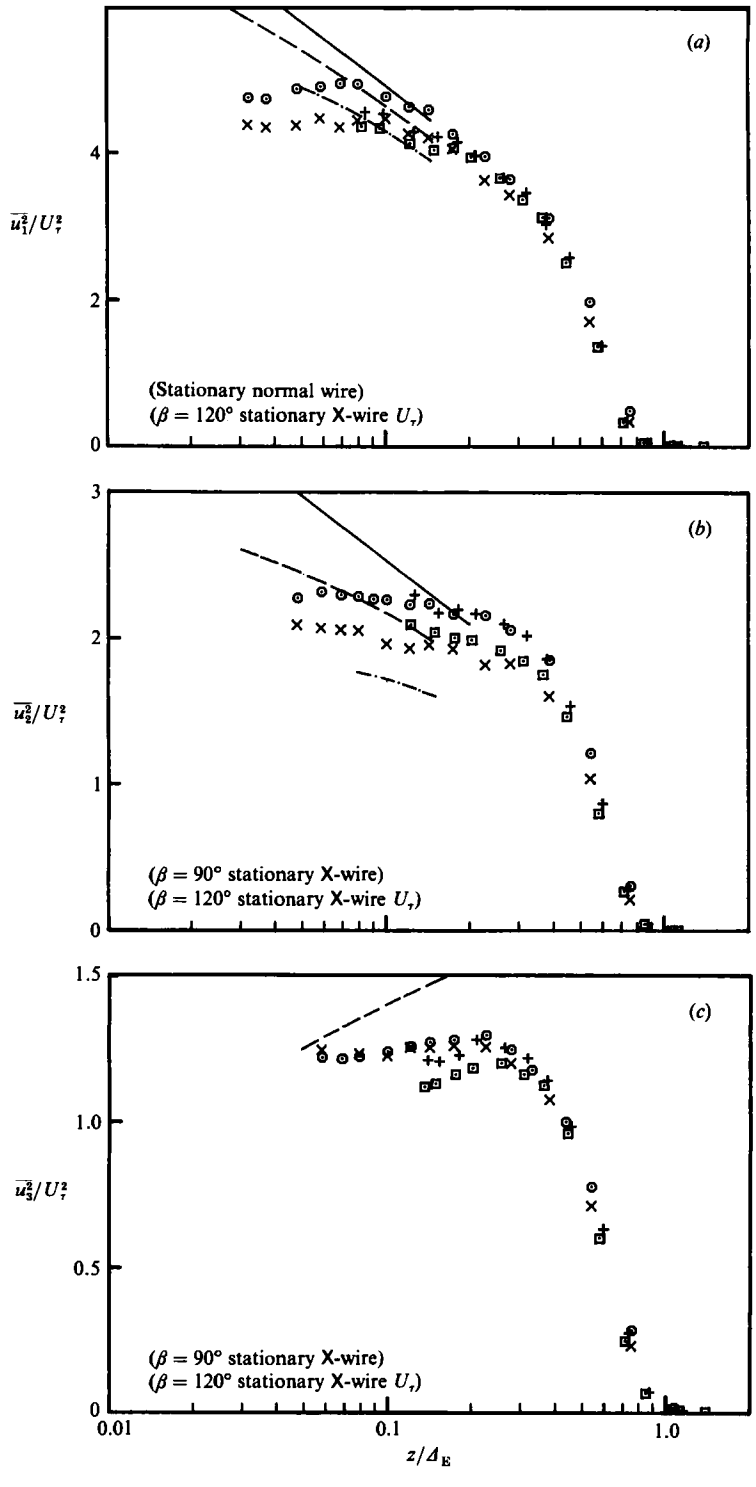

FIGURE 24. Turbulence intensity distributions of (*a*) $\overline{u_1^2}/U_\tau^2$, (*b*) $\overline{u_2^2}/U_\tau^2$ and (*c*) $\overline{u_3^2}/U_\tau^2$ over the mesh roughness, K_τ: +, 1413; ⊡, 2957; ×, 3484; ⊙, 6841. Predicted distributions (equations (4) and (5)) K_τ: ——, $\to\infty$; –·–·–, 1413; – – – –, 6841.

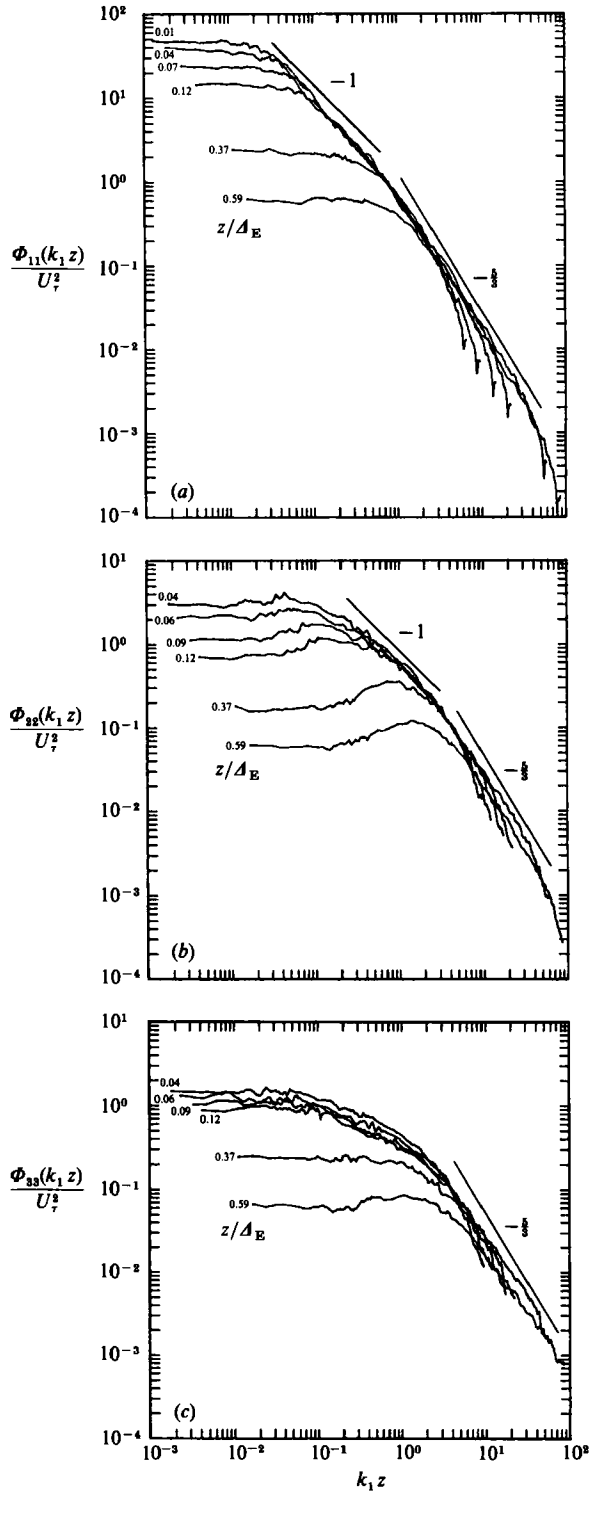

FIGURE 25. Smooth-wall spectra for varying z/Δ_E in the fully turbulent region. Inner-flow scaling. $K_\tau = 4787$. (*a*) u_1-spectra, (*b*) u_2-spectra, (*c*) u_3-spectra.

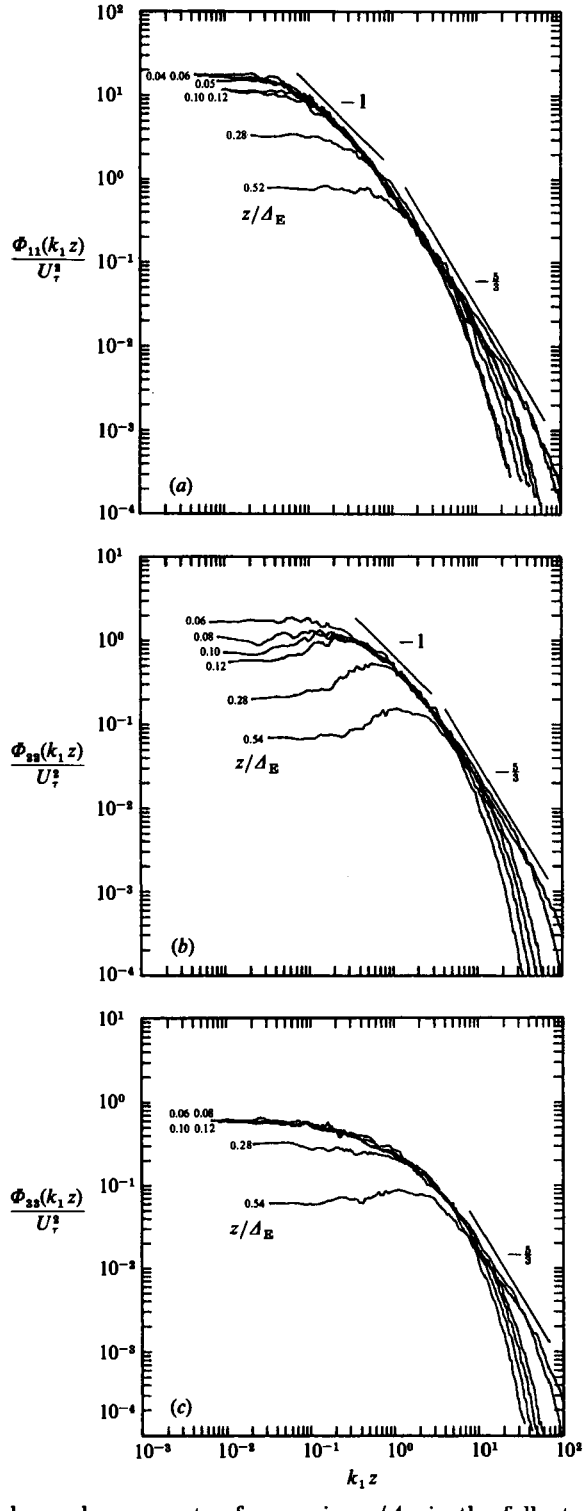

FIGURE 26. Mesh roughness spectra for varying z/Δ_E in the fully turbulent region. Inner-flow scaling. $K_\tau = 6841$. (*a*) u_1-spectra, (*b*) u_2-spectra, (*c*) u_3-spectra. ($\beta = 120°$ stationary X-wire U_τ).

Here the fully turbulent region is defined as $100\nu/U_\tau < z < \Delta_E$ for a smooth wall and $2k < z < \Delta_E$ for a rough wall. Figure 25(*a–c*) shows the smooth-wall u_1-, u_2- and u_3-spectra respectively, measured in the fully turbulent region for various values of z/Δ_E at the highest value of $K_\tau = 4787$. The u_1-, u_2- and u_3-spectra each appear to follow (15). For z/Δ_E sufficiently small an inverse-power-law region emerges in the u_1- and u_2-spectra, while no such region can be seen in the u_3-spectra. This behaviour is consistent with the model of Perry & Chong (1982) and of Perry *et al.* (1986). At high wavenumbers the spectra collapse to a $-\frac{5}{3}$ power law and this is consistent with Kolmogorov's analysis of the spectrum in the inertial subrange. When plotted with Kolmogorov scaling coordinates, each of the above spectra collapse and an inertial subrange is evident. In the 'wake region' spatial resolution is less of a problem because the Kolmogorov lengthscales are considerbly larger than those in the turbulent wall region. Figure 26 (*a–c*) shows the mesh roughness u_1-, u_2- and u_3-spectra respectively, measured at the highest value of $K_\tau = 6841$. These spectra are similar to the corresponding smooth-wall spectra. The smooth- and rough-wall spectra give support to Townsend's Reynolds-number similarity hypothesis and to the model of Perry *et al.* (1986).

5. Conclusions

In spite of the major experimental difficulties encountered with hot-wire anemometry, the spectral and turbulence-intensity data measured in smooth- and rough-walled boundary layers presented here give encouraging support for the attached-eddy hypothesis of Townsend, the model of Perry & Chong and the classic Kolmogorov theory for local isotropy. This complements the work of Perry *et al.* (1986) who confined their measurements to fully developed smooth-walled pipe flow. However, for a completely satisfactory verification of any of the proposed similarity laws, certain problems still need to be overcome. For spectra, the spread in convection velocity is a problem at low wavenumbers and spatial resolution is a problem at high wavenumbers. Large errors were observed in the measurements of Reynolds shear stress with a X-wire above a rough surface. The cause of this was traced to the fact that the spread in the angle of the velocity vectors resolved in the (x, z)-plane approaching a X-wire above a rough surface is very large, whereas on a smooth surface the angular spread is sufficiently small so as not to cause difficulties. One method of overcoming this problem is to increase the included angle of the X-wires. This improves measurements of Reynolds shear stress but the errors in the normal fluctuating component (u_3) are greatly increased. It is expected that angular spread in the (x, y)-plane is larger than that in the (x, z)-plane and may be responsible for the cross-contamination of the measurements of $\overline{u_3^2}$, even above a smooth surface. A better solution to the problem is to 'fly' the X-wires, thereby reducing the angular spread in both planes of velocity vectors approaching the probe and at the same time, hopefully, minimizing the effect of cross-contamination. So far, we have studied the effect of 'flying' the wires only on Reynolds shear stress measurements above rough surfaces. We feel that to reduce the cone angle sufficiently in the (x, y)-plane we need to 'fly' the wires at an even higher velocity than is possible with the present apparatus before accurate measurements of $\overline{u_3^2}$ and $\overline{u_2^2}$ may be made. The technique of flying the wires could also be extended to the measurement of turbulence spectra. The fractional spread in convection velocities of various Fourier components would be reduced significantly if the additional bias velocity imposed on the probe is sufficiently large,

thus reducing the uncertainties in the inferred wavenumbers for spectra, especially at low wavenumber.

The authors wish to acknowledge the financial assistance of the Australian Research Grants Scheme and the computer software development by Dr M. S. Chong.

REFERENCES

ABELL, C. J. 1974 Ph.D. thesis, University of Melbourne, Australia.

ACHARYA, M. E. & ESCUDIER, M. P. 1984 BBC Brown Boveri and Co. Ltd. *Report KLR* 84-179C.

ANDREOPOULOS, J. & BRADSHAW, P. 1981 *Boundary-Layer Met.* **20**, 201–213.

ANTONIA, R. A. & LUXTON, R. E. 1971 *J. Fluid Mech.* **48**, 721–761.

BATCHELOR, G. K. 1953 *Theory of Homogeneous Turbulence.* Cambridge University Press.

BREMHORST, K. & BULLOCK, K. J. 1970 *Trans. ASME* C: *J. Heat Transfer* **13**, 1313–1329.

BREMHORST, K. & WALKER, T. B. 1973 *J. Fluid Mech.* **61**, 173–186.

BULLOCK, K. J., COOPER, R. E. & ABERNATHY, F. H. 1978 *J. Fluid Mech.* **88**, 585–608.

CHAMPAGNE, F. H., SLEICHER, C. A. & WEHRMANN, O. H. 1967 *J. Fluid Mech.* **28**, 152–175, 177–182.

CLAUSER, F. H. 1954 *J. Aero. Sci.* **21**, 91–107.

COLES, D. E. 1962 United States Air Force project *RAND Report* R-403-PR.

COLES, D. E. 1968 *Proc. Computation of Turbulent Boundary Layers, Stanford* (ed. D. E. Coles & E. A. Hirst).

ERM, L. P., SMITS, A. J. & JOUBERT, P. N. 1986 *Turbulent Shear Flows* (ed. F. Durst, B. E. Launder, J. L. Lumley, F. W. Schmidt & J. H. Whitelaw), vol. 5. Springer.

GUPTA, A. K. & KAPLAN, R. E. 1972 *Phys. Fluids* **15**, 981–985.

HAMA, F. R. 1954 *Trans. SNAME* **62**, 333–358.

HANCOCK, P. E. & BRADSHAW, P. 1983 *Trans. ASME* I: *J. Fluids Engng* **105**, 284–289.

HENBEST, S. M. 1983 Ph.D. thesis, University of Melbourne, Australia.

HINZE, O. J. 1975 *Turbulence*, 2nd edn. McGraw Hill.

HOOPER, J. D. & HARRIS, R. W. 1982 *Austral. Atomic Energy Commission Report* no. E516.

HUNT, I. A. & JOUBERT, P. N. 1979 *J. Fluid Mech.* **91**, 633–659.

KAWAL, J. G., SHOKR, M. & KEFFER, J. F. 1983 *J. Fluid Mech.* **133**, 83–112.

KLEBANOFF, P. S. 1954 *NACA TN* 3178.

KLEBANOFF, P. S. & DIEHL, Z. W. 1951 *NACA TN* 2475.

KLINE, S. J., REYNOLDS, W. C., SCHRAUB, F. A. & RUNSTADLER, P. W. 1967 *J. Fluid Mech.* **30**, 741–773.

KOLMOGOROV, A. N. 1941 *Dokl. Akad. Nauk SSSR* **30**, 301–305.

LAUFER, J. 1954 *NACA Rep.* 1174.

LAWN, C. J. 1971 *J. Fluid Mech.* **48**, 477–505.

LIM, K. L. 1985 Ph.D. thesis, University of Melbourne, Australia.

MULHEARN, P. J. 1978 *Phys. Fluids* **21**, 1113–1115.

MURLIS, J., TSAI, H. M. & BRADSHAW, P. 1982 *J. Fluid Mech.* **122**, 13–56.

PERRY, A. E. 1982 *Hot-Wire Anemometry.* Clarendon Press.

PERRY, A. E. & ABELL, C. J. 1977 *J. Fluid Mech.* **79**, 785–799.

PERRY, A. E. & CHONG, M. S. 1982 *J. Fluid Mech.* **119**, 173–217.

PERRY, A. E., HENBEST, S. M. & CHONG, M. S. 1986 *J. Fluid Mech.* **165**, 163–199.

PERRY, A. E. & JOUBERT, P. N. 1963 *J. Fluid Mech.* **17**, 193–211.

PERRY, A. E., LIM, K. L., HENBEST, S. M. & CHONG, M. S. 1983 *Fourth Symp. On Turbulent Shear Flows, Karlsruhe, Germany*, pp. 1.13–1.17.

PERRY, A. E., SCHOFIELD, W. H. & JOUBERT, P. N. 1969 *J. Fluid Mech.* **37**, 383–413.

Sabot, J. & Comte-Bellot, G. 1976 *J. Fluid Mech.* **74**, 767–796.
Sabot, J., Saleh, I. & Comte-Bellot, G. 1977 *Phys. Fluids* **20**, S150–S155.
Taylor, G. I. 1938 *Proc. R. Soc. Lond.* A **164**, 476–490.
Tchen, C. M. 1953 *J. Res. Natl Bureau Standards* **50**, 51–62.
Townsend, A. A. 1961 *J. Fluid Mech.* **11**, 97–120.
Townsend, A. A. 1976 *The Structure of Turbulent Shear flow.* Cambridge University Press.
Tutu, N. K. & Chevray, R. 1975 *J. Fluid Mech.* **71**, 785–800.
Watmuff, J. H., Perry, A. E. & Chong, M. S. 1983 *Expts in Fluids* **1**, 63–71.
Willmarth, W. W. & Bogar, T. J. 1977 *Phys. Fluids* **20** (10), Pt 2, S9–S21.
Wills, J. A. B. 1964 *J. Fluid Mech.* **20**, 417–32.
Wyngaard, J. C. 1968 *J. Sci. Instrum.*, Ser. 2, **1**, 1105–1108.